Intelligent Medicine 3 (2023) 104–114

Contents lists available at ScienceDirect

Intelligent Medicine

journal homepage: www.elsevier.com/locate/imed

Research Article

Fluid–structure interaction simulation of pathological mitral valve dynamics in a coupled mitral valve-left ventricle model

Li Cai [1,2], Tong Zhao [1,*], Yongheng Wang [1], Xiaoyu Luo [3], Hao Gao [3,*]

[1] NPU-UoG International Cooperative Lab for Computation and Application in Cardiology, School of Mathematics and Statistics, Northwestern Polytechnical University, Xi'an, Shaanxi 710129, China

[2] Xi'an Key Laboratory of Scientific Computation and Applied Statistics, Xi'an, Shaanxi 710129, China

[3] School of Mathematics and Statistics, University of Glasgow, Glasgow, G128QQ, United Kingdom

ARTICLE INFO

Keywords:
Mitral valve
Left ventricle
Valve disease
Hybrid immersed boundary/finite element method
Calcification
Hypertrophic cardiomyopathy

ABSTRACT

Background Understanding the interaction between the mitral valve (MV) and the left ventricle (LV) is very important in assessing cardiac pump function, especially when the MV is dysfunctional. Such dysfunction is a major medical problem owing to the essential role of the MV in cardiac pump function. Computational modelling can provide new approaches to gain insight into the functions of the MV and LV.

Methods In this study, a previously developed LV–MV model was used to study cardiac dynamics of MV leaflets under normal and pathological conditions, including hypertrophic cardiomyopathy (HOCM) and calcification of the valve. The coupled LV–MV model was implemented using a hybrid immersed boundary/finite element method to enable assessment of MV haemodynamic performance. Constitutive parameters of the HOCM and calcified valves were inversely determined from published experimental data. The LV compensation mechanism was further studied in the case of the calcified MV.

Results Our results showed that MV dynamics and LV pump function could be greatly affected by MV pathology. For example, the HOCM case showed bulged MV leaflets at the systole owing to low stiffness, and the calcified MV was associated with impaired diastolic filling and much-reduced stroke volume. We further demonstrated that either increasing the LV filling pressure or increasing myocardial contractility could enable a calcified valve to achieve near-normal pump function.

Conclusion The modelling approach developed in this study may deepen our understanding of the interactions between the MV and the LV and help in risk stratification of heart valve disease and *in silico* treatment planning by exploring intrinsic compensation mechanisms.

1. Introduction

Valvular heart disease is among the leading diseases affecting average life expectancy and quality of life [1]. Mathematical models are important means of understanding the mechanism of valvular dysfunction and its impact on ventricular pump function. Standalone biomechanical mitral valve (MV) modelling has evolved over decades, ranging from simplified two-dimensional (2D) approximations to three-dimensional (3D) models and to multi-physical/multi-scale models [2]. However, owing to the complex interactions among the MV, heart wall, and blood flow, there has been a lack of studies on the interactions of the MV and ventricular dynamics, and only a few studies have integrated the MV and left ventricle (LV) into a single model [3–6] mathematical modelling of the cardiovascular system [2,7].

With the rapid development of non-invasive clinical imaging technologies [8] including 2D/3D ultrasound, computerized tomography (CT), and nuclear magnetic resonance, realistic 3D shapes and multi-physical models have been widely used in MV modelling [9–10]. Early studies usually used idealized geometries with isotropic material models with either rigidly fixed ventricle [11] or mounted in tubes or structure-only [12]. Although advances have been made in individual MV [2] and LV [13] computational models, the development of a complete MV–LV model is still very challenging. Wong VM, et al. [3] reported a structure-only MV–LV model using LS-DYNA, which included the LV, MV, and chordae tendinae. This model was later extended to study stress dis-

* Corresponding authors: Tong Zhao, NPU-UoG International Cooperative Lab for Computation and Application in Cardiology, School of Mathematics and Statistics, Northwestern Polytechnical University, Xi'an, Shaanxi 710129, China (Email: zhaotong123@mail.nwpu.edu.cn); Hao Gao, School of Mathematics and Statistics, University of Glasgow, Glasgow, G128QQ, United Kingdom (Email: Hao.Gao@Glasgow.ac.uk).

https://doi.org/10.1016/j.imed.2022.06.005
Received 5 April 2022; Received in revised form 8 May 2022; Accepted 6 June 2022

tribution at medium pressure using saddle-shaped asymmetrical mitral valvuloplasty rings. A more complete whole-heart model was recently developed using a human cardiac function simulator by the Dassault Systems Living Heart Project [14]; this model consisted of four ventricles, heart valves, electrophysiology, and detailed muscle fibres and collagen structures. Using the same Living Heart model, Rausch, et al. [6] studied the effects of different mitral annulus on cardiac function. Recently, a structure-only LV-MV model was developed to investigate the relationship between infarction geometry and ischaemic mitral regurgitation grade [15]. However, these models did not included fluid–structure interaction (FSI); thus, haemodynamic performance could not be assessed.

Early studies found that even in a fixed U-shaped ventricle, the flow pattern was quite different from that estimated using a tubular geometry model [11]. The earliest valve–heart coupling models including FSI were attributed to pioneering work on the immersed boundary method (IBM) developed by Peskin and McQueen in the 1970s [16–17]. Since then, the IBM has been successfully applied to MV dynamics modelling, for example, the "pseudo-fibre"-based MV model [18–19] and the "finite-element"-based MV model [20–22] with a transversely isotropic material model, which could be calibrated from experimentally measured stiffness data. Other FSI MV models using smoothed-particle hydrodynamics have been developed; these include the model [23–24], which studied the function of the chordae tendinae structure, and studied MV regurgitation [5]. Chandran and Kim [25] reported a prototype of fluid–structure-coupled MV dynamics in a simplified LV model during diastolic congestion using an immersive interface approach. One of the key limitations of such coupled models is that they use a simplified representation of the biomechanics of the LV wall. Using a hybrid immersed boundary (IB)/finite element (FE) method, we have developed a complete MV–LV FSI model derived from an *in vivo* magnetic resonance imaging (MRI) scan of a healthy volunteer [4] with FE representations of both the MV and the LV. The MV part of this model is similar to that study [20], and the LV part was calibrated in a series of studies using clinical measurements [26–27]. We demonstrated that the developed IB/FE MV–LV model could well predict LV pump function and MV dynamics. However, the impact of a diseased valve on cardiac pump function has not previously been studied using this coupled MV–LV model.

In the present study, we build upon our previous study using a coupled FSI MV–LV model [4] to study LV pump function under pathological MV conditions, including one case with occlusion caused by hypertrophic cardiomyopathy (HOCM) and another case with a calcified MV. HOCM is a hereditary disease characterized by an increase in myocardial mass, especially in the diaphragm and the LV wall, and papillary muscle hypertrophy. It can lead to severe LV outflow obstruction and mitral insufficiency and impedes blood flow through the aortic valve, and is associated with a high rate of sudden death [28–29]. A calcified valve results from deposits of calcium in valve leaflets; this usually leads to a much stiffer material property of the leaflets [30] and eventually results in stenosis (narrowing) of the MV [31]. MV stenosis can lead to increased resistance to blood flow and increased heart work and may also cause sudden cardiac arrest [32–33].

2. Methods

The coupled MV–LV model was adapted from our previous work [4], which was based on an MRI study of a healthy volunteer (male, age 28) carried out at the British Heart Foundation Centre, University of Glasgow. The MRI study was approved by the local NHS Research Ethics Committee, and written informed content was obtained before the MRI scan. Details of the MRI protocols can be found in [4,18]. Figure 1 shows the coupled MV–LV geometry consisting of the inflow/outflow tracts, the annulus, the anterior and posterior MV leaflets, 16 chordae tendinae, and the LV. Eight chordae tendinae attach to the anterior leaflet on one side and to one of the papillary muscles on the other side. The thickness of the MV leaflets is around 0.1 cm, and they are divided into 154,000 tetrahedral elements. The 16 chordae tendinae are discretized into 4,707 tetrahedral elements. Details of the reconstruction of the MV including the chordae tendinae from MRI [18,20], and the LV geometry were line with the previous reports [34]. The standalone MV [18,20], the LV model [27], and the coupled MV–LV model [4] have all been previously validated with MRI measurements from the healthy volunteer and the results further compared with values reported in the literature.

2.1. The IB/FE method

The coupled MV–LV model was implemented using the IB/FE approach [35]. Specifically, the blood is described in an Eulerian form and considered to be viscous and incompressible, whereas the immersed solid (i.e., the LV and MV) is described in a Lagrangian form. In detail, the physical domain occupied by the fluid-structure system is denoted Ω, the fixed physical (Eulerian) coordinates are denoted

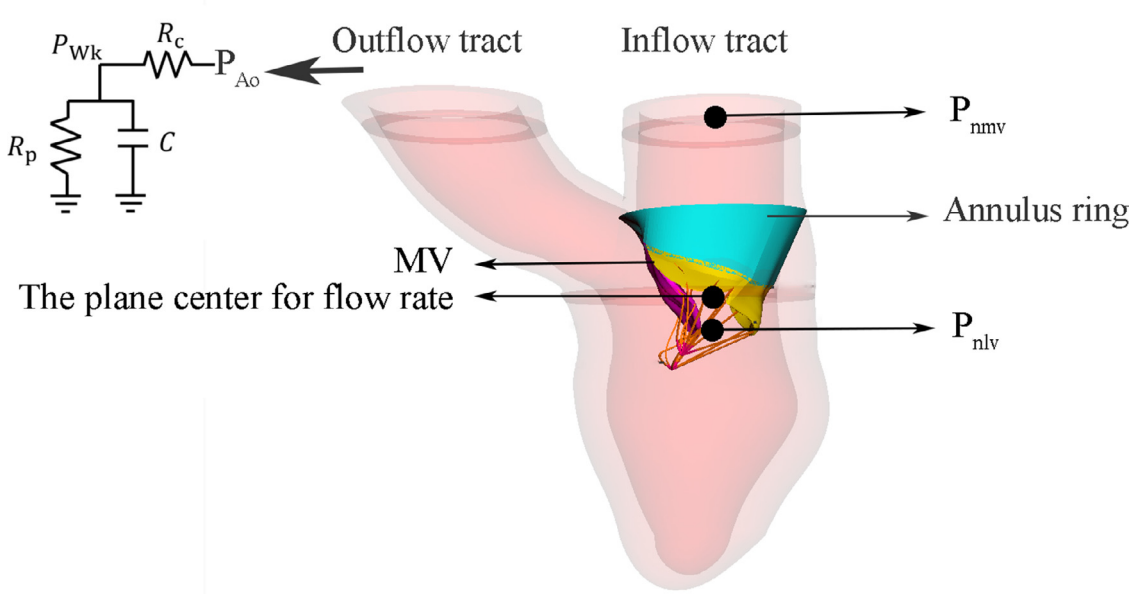

Figure 1. The patient-specific MV–LV model with a three-element Windkessel model attached to the outflow tract [4].

$\mathbf{x} = (x_1, x_2, x_3) \in \Omega$, and the reference configuration of the immersed solid is denoted U with $\mathbf{X} = (X_1, X_2, X_3)$ as the material (Lagrangian) coordinates. The exterior unit normal along ∂U in the reference configuration is $\mathbf{N}(\mathbf{X})$. We let $\chi(\mathbf{X}, t) \in \Omega$ denote the physical position of any material point $\mathbf{X}$ at time t, such that $\chi(\mathbf{X}, t) = \Omega^s(t) \in \Omega$ is the physical region occupied by the deformed solid at time t, and the physical region occupied by the fluid at time t is $\Omega^f(t) = \Omega - \Omega^s(t)$. The IB/FE formulation of the FSI system is:

$$\rho\left(\frac{\partial \mathbf{u}}{\partial t}(\mathbf{x}, t) + \mathbf{u}(\mathbf{x}, t) \cdot \nabla \mathbf{u}(\mathbf{x}, t)\right) = -\nabla p(\mathbf{x}, t) + \mu \nabla^2 \mathbf{u}(\mathbf{x}, t) + \mathbf{f}^s(\mathbf{x}, t) \tag{1}$$

$$\nabla \cdot \mathbf{u}(\mathbf{x}, t) = 0 \tag{2}$$

$$\mathbf{f}^s(\mathbf{x}, t) = \int_U \mathbf{F}^s(\mathbf{X}, t)\delta(\mathbf{x} - \chi(\mathbf{X}, t))\mathrm{d}\mathbf{X} \tag{3}$$

$$\frac{\partial \chi(\mathbf{X}, t)}{\partial t} = \int_\Omega \mathbf{u}(\mathbf{x}, t)\delta(\mathbf{x} - \chi(\mathbf{X}, t))\mathrm{d}\mathbf{x} \tag{4}$$

$$\int_U \mathbf{F}^s(\mathbf{X}, t) \cdot \mathrm{V}(\mathbf{X})\mathrm{d}\mathbf{X} = -\int_U \mathbb{P}^s(\mathbf{X}, t) : \nabla_{\mathbf{X}} \mathrm{V}(\mathbf{X})\mathrm{d}\mathbf{X}, \tag{5}$$

where ρ is the blood density, μ is the blood viscosity, $p(\mathbf{x}, t)$ is the Eulerian fluid pressure, $\mathbf{u}$ is the Eulerian velocity, and $\mathbf{f}^s$ is the Eulerian elastic force density. $\mathbb{P}^s$ is the first Piola–Kirchhoff stress tensor of the deformed solid, which can be derived from certain chosen strain energy functions; the more details can be found in Section 2.2. Interactions between the Lagrangian and Eulerian fields are achieved by integral transforms with Dirac delta function kernel $\delta(x) = \delta(x_1)\delta(x_2)\delta(x_3)$. Interested readers are referred to [35] for more details of this hybrid IB/FE framework, and to [4] for the IB/FE implementation of the FSI MV–LV model. Validation of the IB/FE formulation can be found [35] and validation specifically for cardiac mechanics [36].

2.2. Constitutive laws for immersed solid

The total Cauchy stress in this IB/FE system is

$$\sigma(\mathbf{x}, t) = \begin{cases} -p\mathbb{I} + \mu[\nabla \mathbf{u} + (\nabla \mathbf{u})^T] & \text{for } \mathbf{x} \in \Omega^f, \\ -p\mathbb{I} + \mu[\nabla \mathbf{u} + (\nabla \mathbf{u})^T] + \sigma^s(\mathbf{x}, t) & \text{for } \mathbf{x} \in \Omega^s, \end{cases} \tag{6}$$

in which $\mathbb{I}$ is the identity tensor and σ^s is the solid stress tensor, which can be derived from chosen strain energy functions. The first Piola–Kirchhoff stress ($\mathbb{P}^s$) in (5) is related to σ^s by

$$\mathbb{P}^s = (\det \mathbb{F})\, \sigma^s \mathbb{F}^{-T}, \tag{7}$$

where $\mathbb{F} = \partial \mathbf{x}/\partial \mathbf{X}$ is the deformation gradient for the immersed solid.

2.2.1. MV leaflets and chordae

The mechanical properties of the MV leaflets are considered to be hyperelastic, anisotropic, and incompressible [9], as widely assumed in the literature [12,21,37]. Following our previous studies [4,38], the MV leaflets are characterized by the following strain energy function:

$$W_{\mathrm{MV}} = \bar{c}_0(I_1 - 3) + \frac{\bar{c}_1}{2\bar{c}_2}(e^{[\bar{c}_2(\max(I_f^c, 1) - 1)^2]} - 1), \tag{8}$$

where $\bar{c}_0, \bar{c}_1$, and $\bar{c}_2$ are the material parameters, with values adapted from [4]; $I_1 = \mathrm{trace}(\mathbb{C})$ is the first invariant of the right Cauchy–Green deformation tensor $\mathbb{C} = \mathbb{F}^T\mathbb{F}$; $I_f^c = \mathbf{f}_0^c \cdot (\mathbb{C}\mathbf{f}_0^c)$ is the squared stretch along the collagen fibre direction; $\mathbf{f}_0^c$ represents the collagen fibre orientation of the MV leaflets in the reference configuration; and $\mathbf{f}^c = \mathbb{F}\mathbf{f}_0^c$ is the fibre direction in the current state. The max() function ensures that the embedded collagen network only bears loads when stretched, not under compression. The strain energy function for the chordae tendinae is:

$$W_{\mathrm{MCT}} = \bar{a}_1(I_1 - 3), \tag{9}$$

where $\bar{a}_1$ is the material parameter. Similar to [4], we set $\bar{a}_1 = 9{,}000$ kPa in systole and 540 kPa in diastole to account for papillary muscle contraction.

From Equations (8) and (9), the Cauchy stress tensors in the MV leaflets and chordae tendinae are:

$$\sigma_{\mathrm{MV}}^s = \frac{\partial W_{\mathrm{MV}}}{\partial \mathbb{F}}\mathbb{F}^T + \left(\beta_s \log(I_3) - \bar{c}_1\right)\mathbb{I} \tag{10}$$

$$\sigma_{\mathrm{MCT}}^s = \frac{\partial W_{\mathrm{MCT}}}{\partial \mathbb{F}}\mathbb{F}^T + \beta_s \log(I_3)\mathbb{I}, \tag{11}$$

where $I_3 = \det(\mathbb{C})$, β_s is the bulk modulus, used to ensure the incompressibility of the immersed solid, and the whole FSI system is incompressible through Equation (2). Our prior study has shown that this additional penalty term can yield more accurate stresses [34]. The term $\bar{c}_1\mathbb{I}$ is the pressure-like stress that ensures the solid-like stress is zero when $\mathbb{F} = \mathbb{I}$.

In this study, those parameters [4] used to describe a healthy heart are listed in Table 1 and denoted as the normal case. To determine the constitutive parameters for the HOCM valve and the calcified valve, stretch-stress data from the literature were used by solving a least-squares fitting problem following the same approach [38]. In this study, the experimental data for the HOCM valve were obtained from reference [39], and the experimental data for the calcified valve were obtained from reference [30]. The fitting results are shown in Figure 2, and the estimated parameters can be found in Table 1. Both the anterior and posterior leaflets of the calcified MV were much stiffer than those in the normal case or the HOCM case.

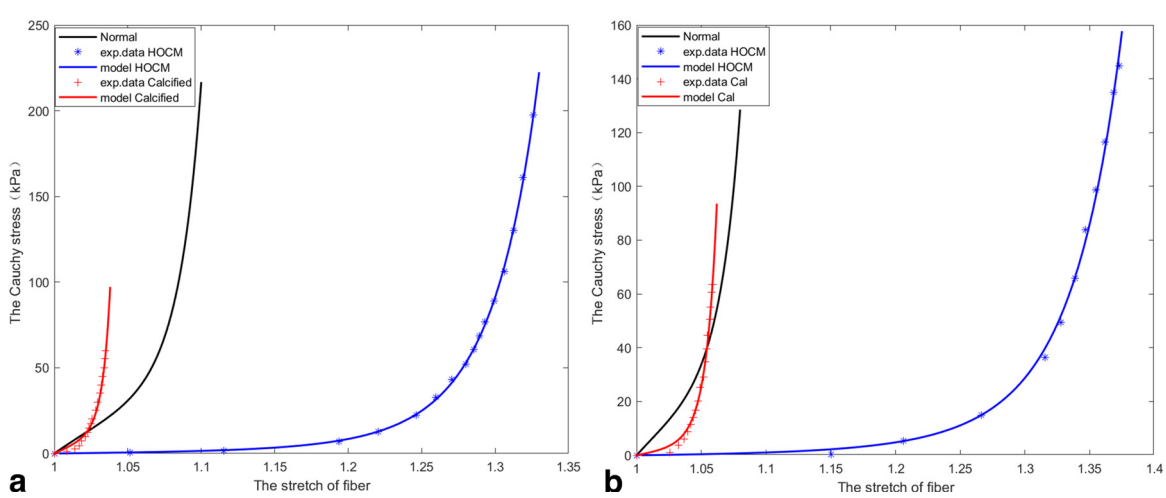

Figure 2. Fitted stretch-stress curves of the anterior (a) and posterior (b) leaflets with selected experimental data.

Table 1 Material parameters for mitral value leaflets and the myocardium in the normal case (kPa)

MV leaflets Case	Values	$\bar{c}_0$	$\bar{c}_1$	$\bar{c}_2$				
Normal	Anterior	17.4	31.3	55.93				
	Posterior	10.2	50.0	63.48				
HOCM	Anterior	0.29	1.78	6.47				
	Posterior	0.03	1.66	4.21				
Calcified	Anterior	18.21	24.85	507.35				
	Posterior	2.5	14.421	189.02				
Myocardium								
a	b	a_f	b_f	a_s	b_s	a_{fs}	b_{fs}	T_{ref}
0.24	5.08	1.46	4.15	0.87	1.6	0.3	1.3	225

2.2.2. Myocardium

The myocardium is regarded as an incompressible, orthotropic nonlinear material [7,34,40]. The constitutive law proposed by Holzapfel and Ogden was used here to describe the passive elastic response of the myocardium [40], that is,

$$W_{\text{myo}} = \frac{a}{2b}\exp\left[b\left(I_1-3\right)\right] + \sum_{\text{i}=\text{f,s}} \frac{a_{\text{i}}}{2b_{\text{i}}}\left\{\exp\left[b_{\text{i}}\left(\max\left(I_{4\text{i}},1\right)-1\right)^2\right]-1\right\} + \frac{a_{\text{fs}}}{2b_{\text{fs}}}\left\{\exp\left[b_{\text{fs}}\left(I_{8\text{fs}}\right)^2\right]-1\right\}, \tag{12}$$

where $a, b, a_f, b_f, a_s, b_s, a_{fs}$, and b_{fs} are material parameters, the parameters associated with a have stress dimension (i.e. kPa), and the parameters related to b are dimensionless. I_{4i} and I_{8fs} $(i = f, s)$ represent the invariants along the fibre and sheet, and their coupling effects, which are further defined below:

$$I_{4\text{f}} = \mathbf{f}_0 \cdot \left(\mathbb{C}\mathbf{f}_0\right), \quad I_{4\text{s}} = \mathbf{s}_0 \cdot \left(\mathbb{C}\mathbf{s}_0\right), \quad I_{8\text{fs}} = \mathbf{f}_0 \cdot \left(\mathbb{C}\mathbf{s}_0\right). \tag{13}$$

Here, $\mathbf{f}_0, \mathbf{s}_0$, and $\mathbf{n}_0$ define the layered fibre structure of the myocardium in the reference configuration. T corresponding vectors in the current configuration are:

$$\mathbf{f} = \mathbb{F}\mathbf{f}_0, \quad \mathbf{s} = \mathbb{F}\mathbf{s}_0, \quad \mathbf{n} = \mathbb{F}\mathbf{n}_0. \tag{14}$$

The active stress of the myocardium is defined as:

$$\mathbb{P}^{\text{a}} = JT\mathbb{F}\mathbf{f}_0 \otimes \mathbf{f}_0, \tag{15}$$

where T is the active systolic force of the LV. This can be calculated by a set of ordinary differential equations [26], such that $T = \mathcal{F}(T_{\text{ref}}, \text{Ca}^{2+}, \lambda, \dot{\lambda}, t)$, where T_{ref} is the isomeric contractility, λ is the stretch, $\dot{\lambda}$ is the stretch rate, Ca^{2+} is the intracellular transient, and t is the time. Parameter values for Equations (12) and (15) can be found in Table 1. These were inversely determined by matching measured *in vivo* LV pump function of the healthy volunteer; details can be found [4].

2.3. Numerical implementation and boundary conditions

In the numerical simulation, the coupled MV–LV model was immersed in a 17 cm × 16 cm × 16.5 cm fluid domain discretized into a regular 80 × 80 × 80 Cartesian grid. A basic time step size $t_0 = 1.22 \times 10^{-5}$ s was used in the diastolic and relaxation phases, a reduced time step size $(0.25t_0)$ was used in the early systole with a duration of $0.1s$, and an even smaller time step of $0.125t_0$ was used in the remainder of the systolic phase, following our previous study [27], owing to the rapid increase in blood pressure in systole. Note that the change of time step did not affect the simulation results; similar adaptive time-stepping approaches [41] have been widely used in computational fluid dynamics for controlling accuracy and enhancing efficiency. The numerical implementation was based on the IBAMR software infrastructure (https://ibamr.github.io/), which is a distributed-memory parallel implementation of the IBM with support for Cartesian grid adaptive mesh refinement. Details of spatial and temporal discretization and implementation of the coupled MV–LV model can be found [34–35], and the validation for use in computational biomechanics can be found [36].

Only the MV and LF region can deform, and fluid boundary conditions are applied to the top plane of the inflow and outflow tract [4,27]. During the diastolic period of the ventricle, a linearly increased pressure (from 0 mmHg to 8 mmHg) is applied to the inflow tract plane, and the end-diastolic pressure (EDP) is 8 mmHg. At the same time, we apply an additional pressure P_{endo} to the endocardial surface of the LV, which increases linearly from 0 to 12 mmHg in 0.4 s and then linearly decreases to 0 mmHg at end-diastole in 0.8 s. During contraction, the aortic valve opens and the blood flows out of the LV. At this point, a three-element Windkessl model is coupled to the outflow tract to provide physiologically accurate pressure boundary conditions at the aortic valve. When systolic ejection ends, the Windkessel model disconnects from the outflow tract.

2.4. Haemodynamic parameters for evaluating MV function

To evaluate the haemodynamic performance of the MV function, several haemodynamic parameters were introduced. We denote by V_F the volume of blood flowing into the LV when the MV opens, by V_R the total regurgitant volume to LA when the MV is closing, and by V_L the leakage volume to LA when the AV is opening. They are defined as follows:

$$\text{V}_F = \int_{t_{\text{bd}}}^{t_{\text{ed}}} \mathbf{f}(t)\text{d}t, \tag{16}$$

$$\text{V}_R = \int_{t_{\text{bc}}}^{t_{\text{ec}}} \mathbf{f}(t)\text{d}t, \tag{17}$$

$$\text{V}_L = \int_{t_{\text{ec}}}^{t_{\text{es}}} \mathbf{f}(t)\text{d}t, \tag{18}$$

where $t_{\text{bd}}, t_{\text{ed}}, t_{\text{bc}}, t_{\text{ec}}$, and t_{es} are the beginning of diastole, the end of diastole, the beginning of MV closure, the end of MV closure, and the end of systole, respectively.

The total regurgitant fraction (RF) was [42]

$$\text{RF} = \frac{V_R + V_L}{V_F} \times 100\%. \tag{19}$$

The transvalvular pressure gradient (TPG) is used to measure potential energy loss as the blood passes through valves [43]. During the diastolic phase, the TPG for the MV was:

$$\text{TPG}(t) = P_{\text{nmv}}(t) - P_{\text{nlv}}(t), \tag{20}$$

where P_{nmv} is the blood pressure near the leaflets at the left atrium side, and P_{nlv} is the blood pressure near the leaflets at the LV side. The smaller the TPG, the less energy loss occurs [43]. To evaluate the impedance of the MV to the blood flow, the effective orifice area (EOA) was introduced following [42,44]:

$$\text{EOA} = \frac{Q_{\text{rms}}}{31\sqrt{\Delta P/\rho}}, \tag{21}$$

with

$$Q_{\text{rms}} = \sqrt{\frac{\int_{t_1}^{t_2} Q(t)^2 \text{d}t}{t_2 - t_1}}, \tag{22}$$

where Q_{rms} is the root mean square of the volumetric flow rate, $Q(t)$ is the flow rate through the MV during the diastolic filling phase, $\Delta P = P_{nmv} - P_{nlv}$ denotes the diastolic TPG, and ρ is the blood density.

3. Results

3.1. The normal case

The simulated LV pressure throughout one cardiac cycle is shown in Figure 3a. We also mark four time points: when the LV is at early diastole and the MV starts to open (0.05 s), when the MV is fully opened (0.38 s), at late diastole (0.46 s), and when the MV is fully closed (0.84 s). The LV cavity pressure reached its minimum value at 0.38 s owing to the sucking effect and its maximum value at about 1 s owing to myocardial contraction. Figure 3b shows the flow rates across the MV (red) and the aortic valve (blue) from diastole to systole.

Figure 3c shows the TPGs for the three cases studied. The TPGs of the normal and HOCM valves were similar to each other and much higher than that of the calcified valve. Figure 3d shows the flow rates across the MV for the normal case, the HOCM case, and the calcified case. As the MV gradually opens, rapidly increasing pressure in the LA causes blood to flow from the LA into the LV during diastole. At the MV opening stage, the peak inflow rate in the HOCM case was 386.75 mL/s at 0.26 s, higher than that of the normal valve (281.89 mL/s at 0.38 s) and much higher than that of the calcified valve (156.97 mL/s at 0.41 s). After the MV is closed, there is a small leakage volume due to gaps in the MV. However, as shown in Figure 3d, the valve leakage volume in all three cases was relatively small, i.e. after 0.9 s, whereas the closure regurgitation was much higher in the HOCM case owing to the much softer material property compared with the other two cases (Figure 2).

3.2. Dynamic MV deformation

Figure 4 shows the deformed MV at the four selected time points defined in Figure 3(a). At the time of early diastole, the opening areas of the three MVs were similar. At the moment of the MV being fully opened, the HOCM case had the largest opening area with the largest displacements at the leaflet tips, which could be explained by the very soft material properties. At the time of late diastole, the deformed shapes of the three MVs were again similar, presumably owing to the same boundary conditions being used in the three cases, i.e., the high systolic pressure in the LV. In the fully closed state, the deformed shapes in the three cases were different. For example, the orifice in the normal case was the smallest,the leaflets in the HOCM case substantially bulged into the LA side, and there was the least movement in the calcified case. Table 2 summarizes the average and maximum displacements of the MV for the three cases at the four time points. The valve leaflets in the HOCM case were much greater than those in the other two cases throughout one cardiac cycle. In the fully opened state, the displacement of the MV was relatively large. For example, in the case of HOCM, the maximum displacement reached 1.537 cm, but the displacement of the calcified valve leaflet was 1.148 cm, showing the least motion among the three cases. At the time of late diastole, the average and maximum displacements for the normal and HOCM cases were similar but greater than those in the calcified case. At the time of the MV being fully closed, the displacements for the normal and HOCM cases were again slightly

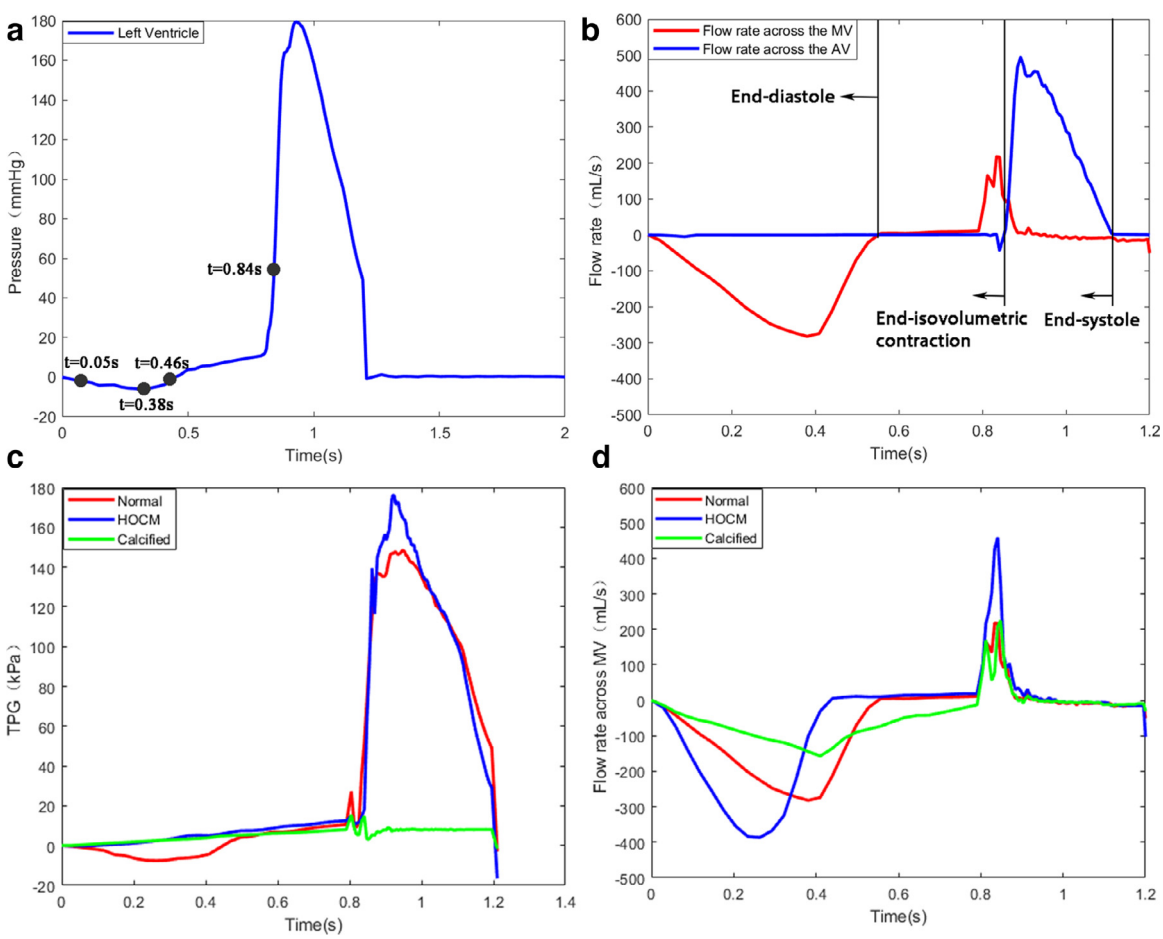

Figure 3. (a) LV pressure profile, (b) flow rates across normal MV and AV, (c) TPG, and (d) transmitral flow rate profiles for the three cases.

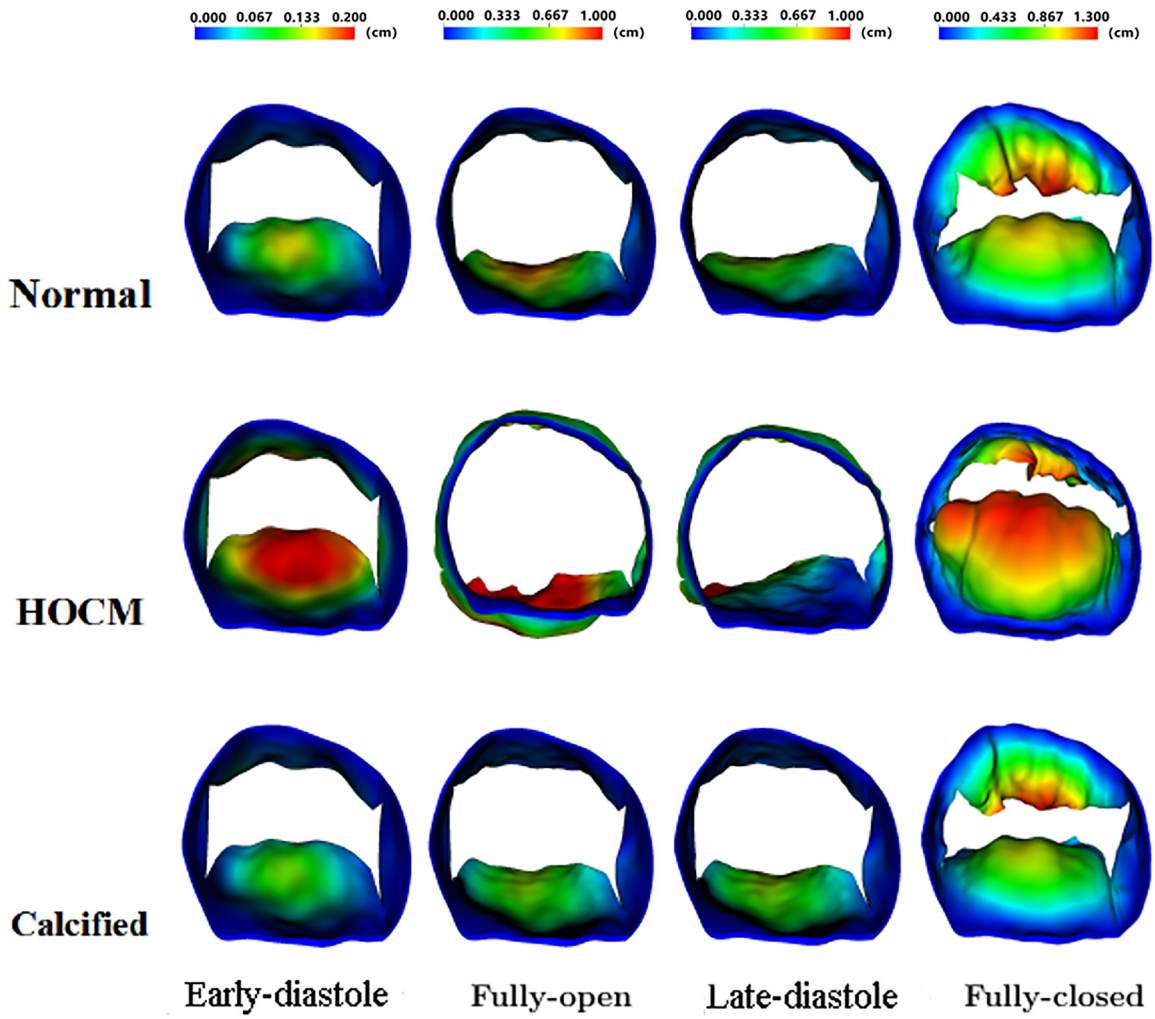

Figure 4. Dynamic deformation of the MV leaflets. The time points from left to right are 0.05 s, 0.38 s, 0.46 s, and 0.84 s.

Table 2 Average and maximum displacements of the mitral valve at different times (cm)

	Average displacement				Maximum displacement			
Case	t=0.05 s	t=0.38 s	t=0.46 s	t=0.84 s	t=0.05 s	t=0.38 s	t=0.46 s	t=0.84 s
Normal	0.018	0.305	0.321	0.363	0.152	1.487	1.576	1.731
HOCM	0.039	0.458	0.381	0.462	0.219	1.537	1.556	1.791
Calcified	0.016	0.217	0.233	0.240	0.125	1.148	1.171	1.466

larger than those in the calcified case. Thus, the material properties of MV leaflets can significantly affect MV deformation.

3.3. Blood flow pattern

Figure 5 shows the cross-sections of the flow field in the early diastole, fully opened, late diastole, and fully closed states. When the MV has just opened, the blood flows from the left atrium to the LV, and the corresponding flow fields in the three cases were generally similar, as shown in Figure 5a. When the MV is fully opened, the blood flows from the left atrium into the LV with a large inflow jet, as shown in Figure 5b. The filling pattern in the calcified case was largely different from those of the other two cases; there was a much higher inflow velocity, whereas the size of the inflow jet was smaller compared with the other two cases, owing to the greatly reduced opening of the MV. At late diastole, a strong inflow jet was still present in the normal and calcified cases, but not in the HOCM case (Figure 5c). The reasons for these different flow patterns were that in the HOCM case, the leaflets were soft and easily closed, and the pressure gradient was small. When the MV was fully closed, the HOCM case showed the most regurgitation (Figure 5d), again owing to the reduced stiffness of the leaflets. Table 3 compares the peak velocity in the three cases. When the MV had just opened, the maximum velocity of the flow field was relatively small. Specifically, the maximum velocity in the HOCM case was 0.17 m/s, whereas the maximum velocities in the normal case and the calcified case were slightly higher. When the MV was fully opened, the maximum velocities of the three valves were much higher than in early diastole; the maximum velocity of the calcified case reached 2.05 m/s, and we observed 1.76 m/s

Table 3 Peak velocities of the transvalvular flow (m/s)

Case	0.05 s	0.38 s	0.46 s	0.84 s
Normal	0.37	1.76	1.49	1.21
HOCM	0.17	1.18	0.73	1.30
Calcified	0.46	2.05	1.94	2.05

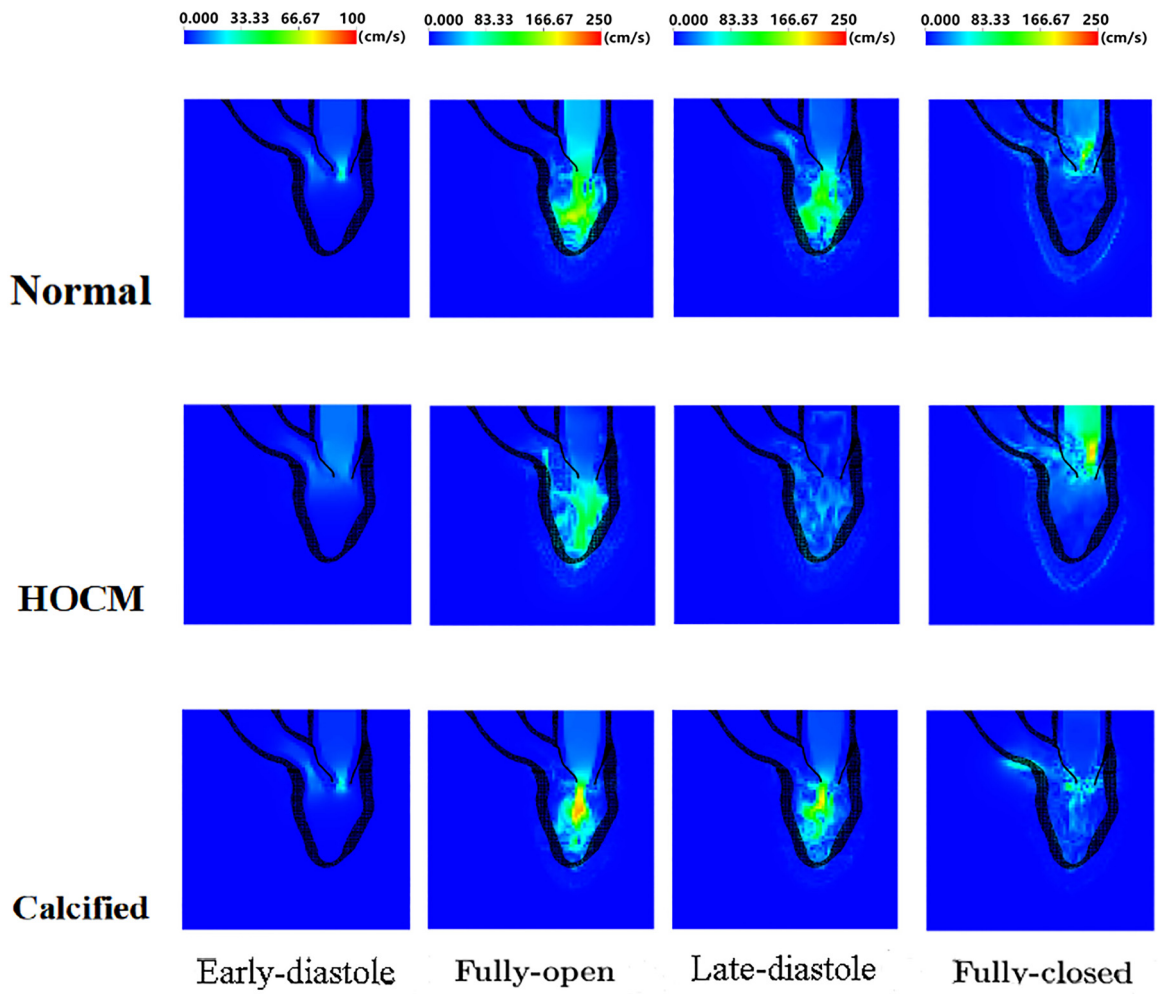

Figure 5. Blood flow patterns in the LV for the three cases. The time points from left to right are 0.05 s, 0.38 s, 0.46 s, and 0.84 s, as defined in Figure 3a.

for the normal case and 1.18 m/s for the HOCM case. At late diastole, the maximum velocity of the normal case and the calcified case were still high (1 m/s), whereas the maximum velocity of the HOCM case was much lower (0.73 m/s). At the time of the MV being in the fully closed state, the relative high velocity is the peak velocity of the regurgitant flow, with the highest value in the calcified case owing to very stiff leaflets and incomplete closure of the leaflets (Figure 4d). Thus, again, different material properties of MV leaflets will further affect the filling and ejecting flow, which will be further explored in Section 3.4.

3.4. Haemodynamic performance of MV

To analyse the haemodynamic performance in the three cases, we determined the values of the following parameters (summarized in Table 4): V_F, V_R, V_L, RF, TPG, and EOA; see Section 3.4 for definitions. Compared with the normal case, the values of V_F, V_R, V_L, RF, and EOA were larger in the HOCM case, except for TPG at diastole. On the contrary, V_F, V_R, and EOA decreased significantly in the calcified case compared with the normal case, and TPG had highest value. The stroke volume in the HOCM and calcified cases were lower than that of normal valves, especially in the calcified case.

3.5. Validation with the literature

The focus of this study was to compare how pathological MV affects the LV pump function and associated haemodynamics using a well-developed MV–LV model with FSI from our previous studies [4]. Thus,

Table 4 Summary of haemodynamic parameters

Case	Normal	HOCM	Calcified
Stroke volume (mL)	71.49	69.49	47.87
V_F (mL)	81.54	87.59	58.64
V_R (mL)	7.06	12.82	5.90
V_L (mL)	3.66	7.59	4.07
RF (%)	13.15	23.30	17.00
TPG at diastole (mmHg)	3.31	0.95	7.20
EOA (cm^2)	2.61	4.88	1.01

RF: regurgitant fraction; EOA: end-diastolic pressure; TPG: transvalvular pressure gradient.

no comprehensive validation was carried out here. For the interesting readers, we now briefly present a validation of the coupled MV–LV model. The standalone IB/FE MV model was developed in [20] from the same MRI study on a healthy volunteer, and we showed that the transvalvular flow and MV leaflet shapes at different cardiac phases agreed well with MRI measures; see Figures 6 and 7 of [20]. The standalone LV model without systemic circulation was developed [45] and validated with clinical measurements, and a later version with systemic circulation was developed [27]. We have demonstrated that the two IB/FE models can match well with clinical data. Finally, we coupled the IB/FE MV and LV model together [4], which again was validated with corresponding measurements [4]. Thus, the normal case in this study is well calibrated based on the acquired MRI data. To our knowledge, this coupled FSI MV–LV model is probably the first such model to be comprehensively calibrated with *in vivo* data. Notably, the normal case

Table 5 Comparison of haemodynamic parameters for the three cases with literature-reported values

Case	Model prediction	Literature values
Normal		
Stroke volume (mL)	71.49	91 ±19 from 76 adult LVs [47]
EF (%)	51.00	57 (MRI measured) [4], and 49-73 [48]
V_F (mL)	81.54	72.10 [49]
V_R (mL)	7.06	7.20 (about 10 % of V_F) [49]
V_L (mL)	3.66	<7.20 (about 10% of V_F) [49]
TPG (mmHg)	3.31	<5.00 [50]
EOA (cm^2)	2.61	2.00-6.00 [51]
HOCM		
Stroke volume (mL)	69.49	39.94 ± 10.67 [52]
EF (%)	50.00	57.17 ± 4.15 [52]
V_R (mL)	12.82	22 ± 16 (MR Grade 1) [53]
RF (%)	23.30	21 ± 10 (MR Grade 1) [53]
TPG (mmHg)	0.95	< 5.00 [42]
EOA (cm^2)	4.88	2.00-6.00 [51]
Calcified		
EF (%)	41.00	57 ± 9* [54], 58 ± 12 [55]
RF (%)	17.00	> mild regurgitation* [54]
TPG (mmHg)	7.20	5.00-10.00 [50], 9 ± 1* [54]
EOA (cm^2)	1.01	1.30 ± 0.30* [54]

∗ Data were extracted from Table 2 of [54], baseline characteristics with ≤ 10 mmHg mitral gradient.

is not completely subject-specific, for example, it does not capture all features of a healthy heart, such as the detailed flow pattern near the valve and heterogeneity of material properties. A fully subject-specific model could be achieved by taking advantage of machine learning approaches, the so-called digital-twin of the heart [46]. Here, we further compare the numerical results of haemodynamic parameters from the three models with values reported in the literature, as shown in Table 5. Note that Table 5 does not provide an exhaustive summary; however, the results shown suggest that predictions from the three cases are consistent with clinical observations.

3.6. Pump function compensation in the calcified case

As shown in Table 4, the pump function was significantly reduced in the calcified case owing to the calcified MV leaflets. For example, the stroke volume was 47.87 mL, much less than that in the normal case (71.49 mL). As discussed, both the EDP and the pressure applied to the endocardial surface can affect the pump function [4]. Considering the much-reduced pump function in the calcified case, we further increased the EDP from 8 mmHg to 16 mmHg in order to achieve a similar cardiac output to that of the normal case to meet the body's blood demands. Table 6 summarizes the simulated results for this calcified case. With the increased EDP, the stroke volume increased from 47.87 mL at 8 mmHg to 68.78 mL at 16 mmHg, close to that of the normal case (71.49 mL), and the TPG was further increased owing to increased EDP. Thus, it seems that increasing the EDP could compensate for reduced LV pump function by increasing the filling volume in diastole.

A further potential compensation mechanism for the myocardium is to increase contractility. In the calcified case, we further increased myocardial contractility by varying T_{ref} from 169 kPa to 226 kPa, 281 kPa, and 337 kPa with an EPD of 14 mmHg. The results are summarized in Table 7. The increase in T_{ref} had little effect on the MV dynamics and the filling volume. For example, the opening area of the calcified MV was about 1.13 cm^2, whereas because of the greatly increased active tension, the stroke volume increased accordingly, resulting in a similar pump function to that of the normal case.

4. Discussion

In this work, the IB/FE method was used to study normal and pathological MVs with a coupled LV–MV model, which included the MV, LV, and other soft tissues with nonlinear hyperelastic constitutive models. We analysed valve dynamics, flow patterns, and various valve-related haemodynamic quantities in normal, HOCM, and calcified valves to assess the performance of the MV. Our results suggest that the significant differences in MV dynamics and LV pump function among these three cases are largely due to the different material properties of the MV leaflets.

Patients with signs and symptoms of heart failure with a normal LV ejection fraction are considered to have diastolic heart failure, which is usually associated with impaired cardiac diastolic work, changes in filling pressure, and reduced diastolic filling volume [56–57]. In the three cases studied here, the diastolic filling volume was 81.54 mL for the normal valve and 87.59 mL for the HOCM valve, but only 58.64 mL for the calcified valve, owing to the stiffness of the valve in the latter case. The largest filling volume was observed for the HOCM valve, owing to the softness of the soft leaflets; moreover, the regurgitation volume was 12.82 mL in this case, higher than that of the normal case (7.06 mL) or the calcified valve (up to 4.07 mL). Thus, valve calcification may be associated with high risk of heart failure owing to the much-reduced diastolic filling volume in such cases. We further simulated the LV dynamics by increasing EDP for the calcified case (Section 3.6). Usu-

Table 6 Haemodynamic parameters of the calcified case with different end-diastolic pressures

Parameters	EDP = 8 mmHg	EDP = 10 mmHg	EDP = 12 mmHg	EDP = 14 mmHg	EDP = 16 mmHg	Normal case
Systolic ejection (ms)	246	246	254	254	254	254
Stroke volume (mL)	47.87	59.63	59.63	64.53	68.78	71.49
V_F (mL)	58.64	64.34	70.37	75.64	79.54	81.54
V_R (mL)	5.90	6.07	6.24	6.51	6.40	7.06
V_L (mL)	4.07	4.39	4.50	4.82	4.84	3.66
RF (%)	17.00	16.26	15.26	14.98	14.13	13.15
TPG (mmHg)	7.20	7.74	8.26	9.00	9.49	3.31
EOA (cm^2)	1.01	0.91	1.14	1.22	1.27	2.61

Table 7 Haemodynamic parameters of calcified MV with varied T_{ref} at p = 14 mmHg

Parameters	T_{ref} = 169 kPa	T_{ref} = 226 kPa	T_{ref} = 281 kPa	T_{ref} = 337 kPa
Systolic ejection (ms)	253	254	261	268
Stroke volume (mL)	56.38	64.53	69.34	73.80
V_F (mL)	75.64	75.64	75.64	75.66
V_R (mL)	5.33	6.51	6.96	7.43
V_L (mL)	4.49	4.82	4.31	3.97
RF (%)	14.47	14.98	14.90	15.07
TPG (mmHg)	8.98	9.00	8.95	8.93
EOA (cm^2)	1.13	1.22	1.13	1.13

ally, an increased EDP is associated with diastolic heart failure [57]. As shown in Table 6, with increasing EDP, the diastolic filling volume increased accordingly, as expected, from 58.64 mL to 79.54 mL, close to the filling volume of the normal case (81.54 mL). The regurgitation volume and leakage volume increased slightly, but the final regurgitation fraction showed a decreasing trend from 17% to 14.13% owing to the much-increased filling volume. Similar results were observed for EOA, which increased from 1.01 cm^2 to 1.27 cm^2. These results suggest that for EDP $\geq$ 14 mmHg, the calcified case can maintain a similar pump function to that of the normal case. Similar results were found for increased contractility, for example, when T_{ref} was increased to 337 kPa, the stroke volume was 73.8 mL, close to that of the normal case. Thus, the coupled MV–LV model allows exploration of various cardiac compensation mechanisms when the heart is dysfunctional, such as in the case of a calcified MV.

Although the predicted pump function of the coupled MV–LV model, in general, agreed with literature reported measurements, the three cases cannot be treated as patient-specific models as all the simulations were deterministic, using material properties from other studies and commonly used boundary conditions owing to the lack of measurements for each case. Therefore, carrying out a direct validation was unfeasible. Instead, we compared our modelling predictions with published data; see Section 3.5. The normal case had the closest results to the *in vivo* measurements from the healthy volunteer; however, various assumptions had to be made when developing this coupled MV–LV model. For example, the chordae tendinae structure was not constructed based on images but was an assumed structure following our previous studies [18]. This was because the chordae tendinae is beyond the resolution of *in vivo* CMR scans. The use of CT scans may partially overcome this resolution issue; however, the radiation risk prevents the use of CT in healthy volunteers [12]. An alternative method is to use a rule-based approach combined with limited image data through topology optimization [58]. Furthermore, the great vessels, the left atrium, and the aortic valve were all simplified. For example, a three-element Windkessel model was used for systemic circulation rather than a closed-loop cardiovascular system or a one-dimensional vessel tree model, which could be used to study how MV dysfunction affects blood flow in both large and peripheral vessels and their feedback to ventricular pump function [27]. The aortic valve was also modelled as a simple diode. Furthermore, constructing a patient-specific left atrium from *in vivo* images would be extremely challenging owing to the complex structure and very thin wall [37,59].

A further challenge was to personalize the MV–LV model based on *in vivo* non-invasive clinical measurements. To calibrate the normal case, we mainly used MRI scans, including cine images at different cardiac phases, myocardial strains, ejection fraction, and transvalvular flow rates [4]. Other measurements will be helpful to further calibrate this model. These include LV pressure, although the use of this measurement is limited by its invasive nature, and transmitral E and A waves, although these require a realistic LA model, in particular for matching the A wave; for a recent study of coupling a realistic MV and an LA [22]. Personalized geometries of LV and MV can be improved owing to advances in clinical imaging technologies and artificial intelligence [60], i.e., by learning geometries directly from clinical images [61]. Inference of mechanical properties in this way is still not fully established; however, estimation of myocardial parameters using *in vivo* imaging data has been reported in various studies [62], including one of ours [26], although very few studies have focused on the MV owing to its complex structure and fast dynamics [2]. For the present study, we did not have access to MRI scans of the HOCM and calcified cases; thus, MV leaflet properties for these cases were estimated using values reported in the literature [30,39], and the LV myocardium was assumed to function similarly to that in the normal case. Future studies will include *in vivo* data from patients with either HOCM or calcified MV. It is expected that a large cohort of patients will be needed to achieve statistical significance.

As we move towards precision medicine guided by high-fidelity patient-specific models [60], it is of paramount importance to quantify the impact of uncertainties in model parameters on the predicted quantities as well as the uncertainty of parameter inference with limited available measurements. Various sources of uncertainties and their importance have been discussed in the seminal paper by Mirams et al. [63], and some recent efforts in computational cardiology can be found in [59,64–65]. As the dimension of the computational model increases, the number of simulations must also increase in order to perform a sensitivity analysis, especially a global sensitivity analysis, such as in the approach of Sobol [66]. In the coupled MV–LV model, the number of model parameters is around 20; given the uncertainties in boundary conditions and geometries, and the fact that one simulation usually takes several days, performing a comprehensive sensitivity analysis directly using the MV–LV model would be very challenging or nearly impossible. To address this problem, surrogate modelling could be used to save computational time; a very successful example is the Gaussian process [59,65]. Furthermore, population-based distributions of model parameters are required to quantify their uncertainties, and such distributions are very sparse in the literature. Thus, a comprehensive sensitivity analysis of the coupled MV–LV model would be beyond the scope of this study. We varied one boundary condition (EDP) and one material property (T_{ref}) in the calcified case (see Section 3.6); this approach is similar to a local sensitivity analysis and sheds light on how certain boundary conditions and material parameters affect model predictions. As shown in Table 6, EDP significantly affected filling volume and transmitral valve flow (V_F, EOA) but not systolic ejection duration. On the contrary, T_{ref} mainly affected systolic ejection duration and stroke volume but not transmitral valve flow; see Table 7. Thus, accurate EDP measurement and reliable inference of T_{ref} are both very important for developing a clinically useful MV–LV model.

In this study, we aimed to study the intricate interactions among the MV, the LF, and blood flow, which have essential roles in cardiac function. A coupled FSI LV–MV model, initially calibrated using data from a healthy volunteer, was used to investigate the dynamic and haemodynamic characteristics of normal, HOCM, and calcified MVs. Our results demonstrated significant differences in MV dynamics and LV pump function among the three cases, largely owing to the different material properties of the MV leaflets. Specifically, the HOCM case showed very bulged MV leaflets at systole because of low stiffness, whereas the calcified MV showed impaired diastolic filling and much-reduced stroke volume. We further found that when the increased LV filling pressure and myocardial contractility were increased, the calcified valve could can achieve a pump function comparable with that of the normal case. Therefore, the coupled MV–LV model, once calibrated, has the potential to be used to explore various cardiac compensation mechanisms when pump function is impaired. Future studies will explore large cohorts of patients to develop personalized computational representations of hearts for risk stratification and treatment optimization.

Conflicts of interest statement

The authors have no conflicts of interest.

Funding

This work was supported by the National Natural Science Foundation of China (Grant Nos.11871399, 12271440) and the UK EPSRC (Grant Nos. EP/S030875, EP/S014284/1, EP/S020950/1, EP/R511705/1, and EP/T017899/1).

Author contributions

Li Cai: Supervision, Project administration, Writing – original draft, Writing – review & editing. **Tong Zhao:** Writing – original draft, Writing – review & editing. **Yongheng Wang:** Visualization. **Xiaoyu Luo:**

Supervision, Project administration. **Hao Gao:** Supervision, Project administration, Writing – original draft, Visualization, Writing – review & editing.

References

[1] Go AS, Mozaffarian D, Roger VL. Heart disease and stroke statistics-2018 update: A Report From the American Heart Association. Circulation 2018;137(12):E493. doi:10.1161/CIR.0000000000000558.

[2] Gao H, Qi N, Feng LY. Modelling mitral valvular dynamics-current trend and future directions. Int J Numer Method Biomed Eng 2016;33(12):E2858. doi:10.1002/cnm.2858.

[3] Wong VM, Wenk JF, Zhang Z. The effect of mitral annuloplasty shape in ischemic mitral regurgitation: a finite element simulation. Ann Thorac Surg 2012;93(3):776–82. doi:10.1016/j.athoracsur.2011.08.080.

[4] Gao H, Feng LY, Qi N. A coupled mitral valve-left ventricle model with fluid-structure interaction. Med Eng Phys 2017;47:128–36. doi:10.1016/j.medengphy.2017.06.042.

[5] Biffi B, Gritti M, Grasso A, et al. A workflow for patient-specific fluid–structure interaction analysis of the mitral valve: A proof of concept on a mitral regurgitation case. Med Eng Phys 2019;74:153–61. doi:10.1016/j.medengphy.2019.09.020.

[6] Rausch MK, Zöllner AM, Genet M. A virtual sizing tool for mitral valve annuloplasty. Int J Numer Method Biomed Eng 2017;33(2):E02788. doi:10.1002/cnm.2788.

[7] Quarteroni A, Lassila T, Rossi S, et al. Integrated heart-coupling multiscale and multiphysics models for the simulation of the cardiac function. Comput Methods Appl Mech Eng 2017;314:345–407. doi:10.1016/j.cma.2016.05.031.

[8] Lamata P, Casero R, Carapella V, et al. Images as drivers of progress in cardiac computational modelling. Prog Biophys Mol Biol 2014;115(2–3):198–212. doi:10.1016/j.pbiomolbio.2014.08.005.

[9] Kunzelman KS, Einstein DR, Cochran R. Fluid-structure interaction models of the mitral valve: function in normal and pathological states. Philos Trans R Soc Lond B Biol Sci 2007;362(1484):1393–406.

[10] Einstein DR, Reinhall P, Nicosia M. Dynamic finite element implementation of nonlinear, anisotropic hyperelastic biological membranes. Comput Methods Biomech Biomed Engin 2003;6(1):33–44. doi:10.1080/1025584021000048983.

[11] Lau K, Diaz V, Scambler P. Mitral valve dynamics in structural and fluid-structure interaction models. Med Eng Phys 2010;32(9):1057–64. doi:10.1016/j.medengphy.2010.07.008.

[12] Wang Q, Sun W. Finite element modeling of mitral valve dynamic deformation using patient-specific multi-slices computed tomography scans. Ann Biomed Eng 2013;41(1):142–53. doi:10.1007/s10439-012-0620-6.

[13] Mangion K, Gao H, Husmeier D, et al. Advances in computational modelling for personalised medicine after myocardial infarction. Heart 2018;104(7):550–7. doi:10.1136/heartjnl-2017-311449.

[14] Baillargeon B, Costa I, Leach JR. Human cardiac function simulator for the optimal design of a novel annuloplasty ring with a sub-valvular element for correction of ischemic mitral regurgitation. Cardiovasc Eng Technol 2015;6(2):105–16. doi:10.1007/s13239-015-0216-z.

[15] Liu H, Narang H, Gorman R, et al. On the interrelationship between left ventricle infarction geometry and ischemic mitral regurgitation grade. In: International Conference on Functional Imaging and Modeling of the Heart. Springer; 2021. p. 425–34.

[16] Peskin C. Flow patterns around heart valves: a numerical method. J Comput Phys 1972;10(2):252–71. doi:10.1016/0021-9991(72)90065-4.

[17] Peskin CS. The immersed boundary method. Acta Numerical 2002;11:479–517.

[18] Ma X, Gao H, Griffith BE. Image-based fluid-structure interaction model of the human mitral valve. Comput Fluids 2013;71:417–25. doi:10.1016/j.compfluid.2012.10.025.

[19] Kaiser AD, McQueen DM, Peskin CS. Modeling the mitral valve. Int J Numer Method Biomed Eng 2019;35(11):e3240. doi:10.1002/cnm.3240.

[20] Gao H, Ma N. A finite strain nonlinear human mitral valve model with fluid-structure interaction. Int J Numer Method Biomed Eng 2014;30(12):1597–613. doi:10.1002/cnm.2691.

[21] Feng LY, Qi N, Gao H. On the chordae structure and dynamic behaviour of the mitral valve. IMA J Appl Math 2018;83(6):1066–91. doi:10.1093/imamat/hxy035.

[22] Feng LY, Gao H, Qi N. Fluid-structure interaction in a fully coupled three-dimensional mitral-atrium-pulmonary model. Biomech Model Mechanobiol 2021;20(4):1267–95. doi:10.1007/s10237-021-01444-6.

[23] Toma M, Bloodworth CH, Pierce EL. Fluid-structure interaction analysis of ruptured mitral chordae tendineae. Ann Biomed Eng 2016;45(3):619–31. doi:10.1007/s10439-016-1727-y.

[24] Toma M, Jensen M, Einstein DR. Fluid-structure interaction analysis of papillary muscle forces using a comprehensive mitral valve model with 3d chordal structure. Ann Biomed Eng 2016;33(4):E02815. doi:10.1007/s10439-015-1385-5.

[25] Chandran KB, Kim H. Computational mitral valve evaluation and potential clinical applications. Ann Biomed Eng 2015;43(6):1348–62. doi:10.1007/s10439-014-1094-5.

[26] Gao H, Aderhold A, Mangion K. Changes and classification in myocardial contractile function in the left ventricle following acute myocardial infarction. J R Soc Interface 2017;14(132):20170203. doi:10.1098/rsif.2017.0203.

[27] Chen WW, Gao H, Luo XY. Study of cardiovascular function using a coupled left ventricle and systemic circulation model. J Biomech 2016;49(12):2445–54. doi:10.1016/j.jbiomech.2016.03.009.

[28] Alexander A, Alexander B, Eugeniy L. Myectomy with mitral valve repair versus replacement in adult patients with hypertrophic obstructive cardiomyopathy: a systematic review and meta-analysis(article). Interact Cardiovasc Thorac Surg 2019;28(28):465–72. doi:10.1093/icvts/ivy269.

[29] Faria B, Loureno M, Azevedo O. Quadricuspid Mitral Valve in Hypertrophic Cardiomyopathy. CASE (Phila) 2020;4(4):240–3. doi:10.1016/j.case.2020.03.007.

[30] Sun W, Pham T. Material properties of aged human mitral valve leaflets. J Biomed Mater Res A 2014;102(8):2692–703. doi:10.1002/jbm.a.34939.

[31] Condello I, Speziale1 G. Mitral Valve Replacement in a Patient with Porcelain Aorta after Previous Myocardial Revascularization. Am J Med Case Rep 2019;7(11):277–9. doi:10.12691/ajmcr-11-4-5.

[32] Fox CS, Vasan RS, Parise H, et al. Mitral annular calcification predicts cardiovascular morbidity and mortality: the framingham heart study. Circulation 2003;107(11):1492–6. doi:10.1161/01.cir.0000058168.26163.bc.

[33] Guerrero M, Dvir D, Himbert D, et al. Transcatheter mitral valve replacement in native mitral valve disease with severe mitral annular calcification: results from the first multicenter global registry. JACC Cardiovasc Interv 2016;9(13):1361–71. doi:10.1016/j.jcin.2016.04.022.

[34] Gao H, Wang H, Berry C. Quasi-static image-based immersed boundary-finite element model of left ventricle under diastolic loading. Int J Numer Method Biomed Eng 2014;30(11):1199–222. doi:10.1002/cnm.2652.

[35] Griffith BE, Luo XY. Hybrid finite difference/finite element immersed boundary method. Int J Numer Method Biomed Eng 2016;33(12):E2888. doi:10.1002/cnm.2888.

[36] Land S, Gurev V, Arens S. Verification of cardiac mechanics software: benchmark problems and solutions for testing active and passive material behaviour. Proc Math Phys Eng Sci 2015;471(2184):1–20. doi:10.1098/rspa.2015.0641.

[37] Feng LY, Gao H, Griffith B. Analysis of a coupled fluid-structure interaction model of the left atrium and mitral valve. Int J Numer Method Biomed Eng 2019;35(35):E3254. doi:10.1002/cnm.3254.

[38] Cai L, Wang Y, Gao H. Some effects of different constitutive laws on fsi simulation for the mitral valve. Sci Rep 2019;9(1):12753. doi:10.1038/s41598-019-49161-6.

[39] Port V, Skallerud B, Sommer G. On modelling and analysis of healthy and pathological human mitral valves: Two case studies. J Mech Behav Biomed Mater 2010;3(2):167–77. doi:10.1016/j.jmbbm.2009.05.004.

[40] Holzapfel GA, Ogden RW. Constitutive modelling of passive myocardium:a structurally based framework for material characterization. Philos Trans A Math Phys Eng Sci. 2009;367(1902):3445–75. doi:10.1098/rsta.2009.0091.

[41] John V, Rang J. Adaptive time step control for the incompressible navier–stokes equations. Comput Methods Appl Mecha Engin 2010;199(9–12):514–24. doi:10.1016/j.cma.2009.10.005.

[42] Zhu GY, Ismail MB, Nakao M. Numerical and in-vitro experimental assessment of the performance of a novel designed expanged-polytetrafluoroethylene str=entless bi-leaflet valve for aortic valve replacement. PLoS One 2019;14(1):1–27. doi:10.1371/journal.pone.0210780.

[43] Yoganathan AP, He ZM, Jones SC. Fluid mechanics of heart valves. Annu Rev Biomed Eng 2004;6(0):331–62. doi:10.1146/annurev.bioeng.6.040803.140111.

[44] Wenbin M, Andres C, Raymond M. Fully-coupled fluid-structure interaction simulation of the aortic and mitral valves in a realistic 3d left ventricle model. PLoS One 2017;12(9):1–21. doi:10.1371/journal.pone.0184729.

[45] Gao H, Carrick D, Berry C, et al. Dynamic finite-strain modelling of the human left ventricle in health and disease using an immersed boundary-finite element method. IMA J Appl Math 2014;79(5):978–1010. doi:10.1093/imamat/hxu029.

[46] Niederer SA, Sacks MS, Girolami M, et al. Scaling digital twins from the artisanal to the industrial. Nat Comput Sci 2021;1(5):313–20. doi:10.1038/s43588-021-00072-5.

[47] Cain PA, Ahl R, Hedstrom E, et al. Age and gender specific normal values of left ventricular mass, volume and function for gradient echo magnetic resonance imaging: a cross sectional study. BMC Med Imaging 2009;9(1):1–10. doi:10.1186/1471-2342-9-2.

[48] Clay S, Alfakih K, Radjenovic A, et al. Normal range of human left ventricular volumes and mass using steady state free precession mri in the radial long axis orientation. MAGMA 2006;19(1):41–5. doi:10.1007/s10334-005-0025-8.

[49] Laniado S, Yellin E, Kotler M. A study of the dynamic relations between the mitral valve echogram and phasic mitral flow. Circulation 1975;51(1):104–30. doi:10.1161/01.cir.51.1.104.

[50] Hahn RT. Degenerative mitral stenosis: interpreting the meaning of mean gradient. Eur Heart J 2020;41(45):4329–31. doi:10.1093/eurheartj/ehaa828.

[51] Krim SR, Vivo RP, Patel A. Direct Assessment of Normal Mechanical Mitral Valve Orifice Area by Real-Time 3D Echocardiography. JACC Cardiovasc Imaging 2012;5(5):478–830. doi:10.1016/j.jcmg.2011.06.024.

[52] Huang X, Yue Y, Wang Y, et al. Assessment of left ventricular systolic and diastolic abnormalities in patients with hypertrophic cardiomyopathy using real-time three-dimensional echocardiography and two-dimensional speckle tracking imaging. Cardiovasc Ultrasound 2018;16(1):1–9. doi:10.1186/s12947-018-0142-y.

[53] Spampinato RA, Jahnke C, Crelier G, et al. Quantification of regurgitation in mitral valve prolapse with four-dimensional flow cardiovascular magnetic resonance. J Cardiovasc Magn Reson 2021;23(1):1–12. doi:10.1186/s12968-021-00783-8.

[54] Misumida N, Guerrero M, Pislaru SV. Hemodynamic response to transseptal transcatheter mitral valve replacement in patients with severe mitral stenosis due to severe mitral annular calcification. Catheter Cardiovasc Interv 2021;97(7):E992–E1001. doi:10.1002/ccd.29285.

[55] Hüting J. Mitral valve calcification as an index of left ventricular dysfunction in patients with end-stage renal disease on peritoneal dialysis. Chest 1994;105(2):383–8. doi:10.1378/chest.105.2.383.

[56] Hay I, Rich J, Ferber P. Role of impaired myocardial relaxation in the production of elevated left ventricular filling pressure. Am J Physiol Heart Circ Physiol 2005;288:H1203–8. doi:10.1152/ajpheart.00681.2004.

[57] Zile MR, Baicu CF, Gaasch WH. Diastolic heart failure abnormalities in active relaxation and passive stiffness of the left ventricle. N Engl J Med 2004;350(19):1953–9. doi:10.1056/NEJMoa032566.
[58] Khalighi AH, Rego BV, Drach A, et al. Development of a functionally equivalent model of the mitral valve chordae tendineae through topology optimization. Ann Biomed Eng 2019;47(1):60–74. doi:10.1007/s10439-018-02122-y.
[59] Rodero C, Strocchi M, Marciniak M, et al. Linking statistical shape models and simulated function in the healthy adult human heart. PLoS Comput Biol 2021;17(4):E1008851. doi:10.1371/journal.pcbi.1008851.
[60] Corral-Acero J, Margara F, Marciniak M, et al. The digital twin'to enable the vision of precision cardiology. Eur Heart J 2020;41(48):4556–64. doi:10.1093/eurheartj/ehaa159.
[61] Romaszko L, Borowska A, Lazarus A, et al. Neural network-based left ventricle geometry prediction from cmr images with application in biomechanics. Artif Intell Med 2021;119:102140. doi:10.1016/j.artmed.2021.102140.
[62] Genet M, Lee LC, Nguyen R, et al. Distribution of normal human left ventricular myofiber stress at end diastole and end systole: a target for in silico design of heart failure treatments. J Appl Physiol (1985) 2014;117(2):142–52. doi:10.1152/japplphysiol.00255.2014.
[63] Mirams GR, Pathmanathan P, Gray RA, et al. Uncertainty and variability in computational and mathematical models of cardiac physiology. J Physiol 2016;594(23):6833–47. doi:10.1113/JP271671.
[64] Mirams GR, Niederer SA, Clayton RH. The fickle heart: uncertainty quantification in cardiac and cardiovascular modelling and simulation. Philos Trans Royal Soc A 2020;378(2173).
[65] Lazarus A, Dalton D, Husmeier D, et al. Sensitivity analysis and inverse uncertainty quantification for the left ventricular passive mechanics. Biomech Model Mechanobiol 2022:1–30. doi:10.1007/s10237-022-01571-8.
[66] Sobol IM. Global sensitivity indices for nonlinear mathematical models and their monte carlo estimates. Mathe Comput Simulat 2001;55(1–3):271–80. doi:10.1016/S0378-4754(00)00270-6.